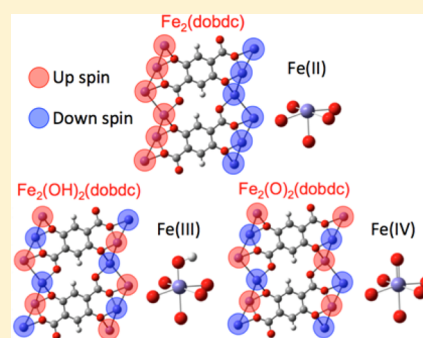


Structural and Electronic Effects on the Properties of $\text{Fe}_2(\text{dobdc})$ upon Oxidation with N_2O Joshua Borycz,^{†,‡} Joachim Paier,^{*,§} Pragma Verma,^{†,‡} Lucy E. Darago,^{‡,||} Dianne J. Xiao,^{‡,||} Donald G. Truhlar,^{*,†,‡} Jeffrey R. Long,^{*,‡,||,⊥,#} and Laura Gagliardi^{*,†,‡}[†]Department of Chemistry, Minnesota Supercomputing Institute, and Chemical Theory Center, University of Minnesota, 207 Pleasant Street SE, Minneapolis, Minnesota 55455-0431, United States[‡]Nanoporous Materials Genome Center, University of Minnesota, 207 Pleasant Street SE, Minneapolis, Minnesota 55455-0431, United States[§]Institut für Chemie, Humboldt-Universität zu Berlin, Unter den Linden 6, 10099 Berlin, Germany^{||}Department of Chemistry, University of California, Berkeley, California 94720-1460, United States[⊥]Department of Chemical and Biomolecular Engineering, University of California, Berkeley, California 94720-1462, United States[#]Materials Sciences Division, Lawrence Berkeley National Laboratory, Berkeley, California 94720, United States

Supporting Information

ABSTRACT: We report electronic, vibrational, and magnetic properties, together with their structural dependences, for the metal–organic framework $\text{Fe}_2(\text{dobdc})$ ($\text{dobdc}^{4-} = 2,5\text{-dioxido-1,4-benzenedicarboxylate}$) and its derivatives, $\text{Fe}_2(\text{O})_2(\text{dobdc})$ and $\text{Fe}_2(\text{OH})_2(\text{dobdc})$ —species arising in the previously proposed mechanism for the oxidation of ethane to ethanol using N_2O as an oxidant. Magnetic susceptibility measurements reported for $\text{Fe}_2(\text{dobdc})$ in an earlier study and reported in the current study for $\text{Fe}^{\text{II}}_{0.26}[\text{Fe}^{\text{III}}(\text{OH})]_{1.74}(\text{dobdc})(\text{DMF})_{0.15}(\text{THF})_{0.22}$, which is more simply referred to as $\text{Fe}_2(\text{OH})_2(\text{dobdc})$, were used to confirm the computational results. Theory was also compared to experiment for infrared spectra and powder X-ray diffraction structures. Structural and magnetic properties were computed by using Kohn–Sham density functional theory both with periodic boundary conditions and with cluster models. In addition, we studied the effects of different treatments of the exchange interactions on the magnetic coupling parameters by comparing several approaches to the exchange–correlation functional: generalized gradient approximation (GGA), GGA with empirical Coulomb and exchange integrals for 3d electrons (GGA+U), nonseparable gradient approximation (NGA) with empirical Coulomb and exchange integrals for 3d electrons (NGA+U), hybrid GGA, meta-GGA, and hybrid meta-GGA. We found the coupling between the metal centers along a chain to be ferromagnetic in the case of $\text{Fe}_2(\text{dobdc})$ and antiferromagnetic in the cases of $\text{Fe}_2(\text{O})_2(\text{dobdc})$ and $\text{Fe}_2(\text{OH})_2(\text{dobdc})$. The shift in magnetic coupling behavior correlates with the changing electronic structure of the framework, which derives from both structural and electronic changes that occur upon metal oxidation and addition of the charge-balancing oxo and hydroxo ligands.



1. INTRODUCTION

The study of magnetic porous materials is interesting because of the many possible lightweight crystalline magnets and their potential applications.¹ Porous materials have been used as molecular magnetic sponges to absorb water² and to improve the sensitivity and efficiency of molecular sensors.^{3,4} Established theories⁵ and trends^{6,7} regarding magnetism within metal–oxide complexes can be used to predict magnetic behaviors of newly discovered or even as-yet unsynthesized materials through the use of quantum mechanical calculations.

One class of porous materials that has garnered considerable attention in the field of magnetism is metal–organic frameworks (MOFs), which consist of metal-containing nodes connected by organic linkers. The tunability and structural diversity of MOFs make them attractive materials for a variety of potential applications. MOFs have been synthesized with

magnetically isolated nodes,⁸ magnetically coupled nodes,^{3,9} flexible pores,¹⁰ very large pore diameters,¹¹ and combinations of these features. The $\text{M}_2(\text{dobdc})$ series, where $\text{M} = \text{Mg}, \text{Mn}, \text{Fe}, \text{Co}, \text{Ni}, \text{Cu}, \text{Zn},$ or Cd , and $\text{dobdc}^{4-} = 2,5\text{-dioxido-1,4-benzenedicarboxylate}$, has been studied extensively for its gas adsorption ability^{12,13} and magnetic properties.¹⁴ Recently, for example, it was shown that $\text{Fe}_2(\text{dobdc})$ can selectively adsorb olefins over paraffins.^{15,16} Upon adsorption of olefins, the magnetic ordering of the $\text{Fe}(\text{II})$ centers changes from ferromagnetic coupling down the one-dimensional chains to antiferromagnetic exchange, which was attributed to enhanced superexchange upon olefin adsorption.^{16,17} Furthermore, there is experimental and computational evidence that suggests that

Received: February 24, 2016

Published: May 2, 2016

$\text{Fe}_2(\text{dobdc})$ exhibits metastable magnetic behavior that is sensitive to temperature, local coordination environment, and the type of guest molecules present in the pores of the MOF.^{16,18}

Four derivatives of $\text{Fe}_2(\text{dobdc})$, namely $\text{Fe}_2(\text{OH})_2(\text{dobdc})$, $\text{Fe}_2(\text{O})_2(\text{dobdc})$, $\text{Fe}_{0.1}(\text{OH})_{0.1}\text{Mg}_{1.9}(\text{dobdc})$, and $\text{Fe}_{0.1}(\text{O})_{0.1}\text{Mg}_{1.9}(\text{dobdc})$, were shown to be involved (in the case of the first named derivative) or postulated to be involved (in the case of the other three) in studies of the catalytic conversion of ethane to ethanol.^{19,20} The compound $\text{Fe}_2(\text{OH})_2(\text{dobdc})$ is a product of the reaction of ethane, N_2O , and $\text{Fe}_2(\text{dobdc})$, which proceeds through $\text{Fe}_2(\text{O})_2(\text{dobdc})$ as a theoretically calculated reactive intermediate.^{19,20} In particular, the high-spin ($S = 2$) character of the $\text{Fe}(\text{IV})$ -oxo species contained within this intermediate was determined to be important for facilitating the ethane oxidation reaction. In order to provide insight into the tunability of the magnetic character of these MOFs, we study here the electronic structure effects resulting from differing metal oxidation states in synthesized $\text{Fe}_2(\text{dobdc})$ and $\text{Fe}_2(\text{OH})_2(\text{dobdc})$ compounds, as well as the highly reactive—and, therefore, fleeting—intermediate $\text{Fe}_2(\text{O})_2(\text{dobdc})$. The parent framework, $\text{Fe}_2(\text{dobdc})$, contains $\text{Fe}(\text{II})$ centers with a quintet ground state, while $\text{Fe}_2(\text{OH})_2(\text{dobdc})$ contains $\text{Fe}(\text{III})$ centers with a sextet ground state, and $\text{Fe}_2(\text{O})_2(\text{dobdc})$ contains $\text{Fe}(\text{IV})$ centers with a quintet ground state.^{19,20}

The change in magnetic ordering upon adsorption of oxygen-containing species (e.g., H_2O) has been investigated previously for many MOFs,^{1,21} and the magnetic properties of $\text{Fe}_2(\text{dobdc})$ with and without bound guests have previously been calculated using both cluster¹⁸ and periodic^{9,14,17} models. Kohn–Sham (KS) density functional calculations that employ local exchange–correlation functionals (local-spin-density approximations, generalized gradient approximations (GGAs), and meta-GGAs) have a tendency to overestimate the magnetic coupling constants between the magnetic centers within $\text{Fe}_2(\text{dobdc})$,^{9,17,18} most likely due to overdelocalization of unpaired spins. To attempt to remediate this, one can use empirical Coulomb and exchange integrals for selected subshells (the $3d$ subshell of Fe in the present work), which is the DFT+U method,²² or one can include a portion of Hartree–Fock exchange^{18,23,24} by using hybrid exchange–correlation functionals. Guidance regarding the value of the U parameter of the DFT+U method or a suitable amount of Hartree–Fock exchange for the calculation of magnetic properties can be sought from previous studies on similar materials^{14,25,26} or from general parametrization of exchange–correlation functionals.

Magnetic MOFs occupy an intermediate position between molecular magnets and bulk transition-metal oxide magnets. In MOFs, one can, in principle, tune the magnetic coupling constants by judicious choice of metal, linker, or both during synthesis and by post-synthetic guest molecule adsorption. Quantum mechanical computations can help to understand the underlying physics behind magnetically ordered MOFs and to predict properties that may currently be inaccessible by synthetic methods. The present work concerns magnetic exchange coupling, which is often quite small in MOFs (for example, 1 – 10 cm^{-1}), and the prediction of such small quantities is difficult. Understanding the capabilities and/or inadequacies of various methods is indispensable when assessing the accuracy of calculations, but the calculation of trends can yield insight even when absolute values show errors.

When performing these calculations on MOFs, one can use either a periodic model or a cluster model. Calculations performed with cluster models can be performed with a wider array of methods, but cluster calculations can be inaccurate if the cluster is too small or must be constrained too tightly.

Here, we report structural and magnetic characteristics of $\text{Fe}_2(\text{dobdc})$, $\text{Fe}_2(\text{O})_2(\text{dobdc})$, and $\text{Fe}_2(\text{OH})_2(\text{dobdc})$ obtained using KS density functional methods with both periodic and cluster models, together with experimental magnetic susceptibility data for $\text{Fe}^{\text{II}}_{0.26}[\text{Fe}^{\text{III}}(\text{OH})]_{1.74}(\text{dobdc})\text{-(DMF)}_{0.15}(\text{THF})_{0.22}$ (where DMF denotes dimethylformamide, and THF denotes tetrahydrofuran). Descriptions of the experimental and computational procedures can be found in section 2, while section 3 provides results and discussion, and section 4 summarizes our conclusions.

2. METHODS

2.1. Preparation and Magnetic Susceptibility Measurements of Hydroxylated $\text{Fe}_2(\text{dobdc})$.

The material $\text{Fe}^{\text{II}}_{0.26}[\text{Fe}^{\text{III}}(\text{OH})]_{1.74}(\text{dobdc})\text{-(DMF)}_{0.15}(\text{THF})_{0.22}$ was prepared by exposure of $\text{Fe}_2(\text{dobdc})$ to excess $\text{N}_2\text{O}(\text{g})$ at $60 \text{ }^\circ\text{C}$. Mössbauer spectroscopy of the resultant material indicated that 87% of the $\text{Fe}(\text{II})$ sites had been oxidized to $\text{Fe}(\text{III})$. Full oxidation to the exact formula $\text{Fe}_2(\text{OH})_2(\text{dobdc})$ could not be achieved without a loss in crystallinity. Elemental analysis of this material indicated that residual amounts of DMF and THF were present in the material. Anal. Calcd for $\text{C}_{9.33}\text{H}_{6.55}\text{Fe}_2\text{N}_{0.15}\text{O}_{8.11}$: C, 30.94; H, 1.82; N, 0.58. Found: C, 30.90; H, 1.60; N, 0.58.

For the sake of convenience, the material $\text{Fe}^{\text{II}}_{0.26}[\text{Fe}^{\text{III}}(\text{OH})]_{1.74}(\text{dobdc})\text{-(DMF)}_{0.15}(\text{THF})_{0.22}$ will be referenced hereafter as $\text{Fe}_2(\text{OH})_2(\text{dobdc})$. Direct current (DC) magnetic susceptibility measurements were performed on $\text{Fe}_2(\text{OH})_2(\text{dobdc})$ under an applied magnetic field of 1000 Oe. Magnetic samples were prepared by adding powdered crystalline compounds to a 7-mm-diameter quartz tube with a raised quartz platform. Solid eicosane was added to cover the samples to prevent crystallite torquing and provide good thermal contact between the sample and the cryogenic bath. The tubes were fitted with Teflon sealable adapters, evacuated on a Schlenk line or using a glovebox vacuum pump, and sealed under vacuum using an H_2/O_2 flame. Following flame sealing, the solid eicosane was melted in a water bath at $40 \text{ }^\circ\text{C}$. Data for $\text{Fe}_2(\text{OH})_2(\text{dobdc})$ were corrected for diamagnetic contributions from the core diamagnetism estimated using Pascal's constants²⁷ to give χ_{D} values of $-0.00027434 \text{ emu/mol}$ and $-0.00024306 \text{ emu/mol}$ (eicosane).

In earlier work on $\text{Fe}_2(\text{dobdc})$,¹⁶ the temperature dependence of the magnetic susceptibility was interpreted using a two-parameter model, the Fisher model,^{28,29} corresponding to a chain of Fe ions interacting with nearest neighbors in the same chain and with Fe ions in z other chains. The parameters are J_{NN} and zJ_{IC} , where J_{NN} is the magnetic coupling of nearest neighbors, and J_{IC} is the magnetic coupling of Fe atoms in different chains. We also attempted to apply this to $\text{Fe}_2(\text{OH})_2(\text{dobdc})$, and the results of this attempt are described in section 3.3.

2.2. Electronic Structure Calculations. **2.2.1. Exchange–Correlation Functionals.** We used several exchange–correlation functionals—in particular, PBE, PBE+U, HSE06, PBE-D2, PBE+U-D2, HSE06-D2, and GAM+U for periodic calculations and PBE, M06-L, PBE0, B3LYP, M06, and HSE06 for cluster calculations. The PBE³⁰ and GAM^{31,32} exchange–correlation functionals are local gradient approximations, and M06-L^{33,34} is a local meta approximation. Because local approximations have a tendency to underestimate band gaps^{25,34–37} and overdelocalize charge distributions,^{38–41} we also employed hybrid approximations that replace a percentage X of local exchange by nonlocal Hartree–Fock exchange. Inclusion of some Hartree–Fock exchange also affects the atomic spin distribution⁴² and geometries.^{42,43} B3LYP,^{44–47} PBE0,^{48,49} and M06⁵⁰ are global hybrids, which means that they use the same percentage X for all

interelectronic separations. PBE0 and B3LYP are global-hybrid gradient approximations with $X = 25$ and 20 , respectively, and M06 is a global-hybrid meta approximation with $X = 27$.

Periodic calculations were performed with plane-wave basis sets with the Vienna Ab initio Simulation Package (VASP).^{51,52} Using global-hybrid functionals for plane-wave calculations can be very expensive. One way to cut the cost^{53,54} is to decrease X to zero at large interelectronic separations; in addition, this decrease is physically justified by the screening of nonlocal exchange by correlation effects at large interelectronic separations.^{55,56} This strategy is used by the HSE06^{53,57–59} range-separated-hybrid gradient approximation, which has $X = 25$ at small interelectronic separation. This decreases the cost, but it is still expensive.

An alternative strategy, with a cost almost the same as local functionals, is to use rotationally invariant empirical modifications of Coulomb and exchange integrals for selected subshells;²² calculations employing this modification with PBE are labeled PBE+U, and calculations employing this strategy with the GAM functional are called GAM+U. (The +U method of ref 22 that is used here is specified in VASP by using LDAUTYPE = 1.) For all the PBE+U and GAM+U calculations reported here, we empirically modified only the $3d$ subshells of the Fe centers, for which we used literature values^{14,60} of 4 and 1 eV, respectively, for the Coulomb (U) and exchange (J) parameters.

In some calculations, a damped-dispersion molecular-mechanics term⁶¹ was also added, and these are labeled as PBE-D2, PBE+U-D2, and HSE06-D2 calculations. The van der Waals R_0 and C_6 parameters determined by Grimme were used in the D2 terms; in particular, the global scaling parameter ($s_6 = 0.75$) fitted for PBE was used for PBE and PBE+U calculations, and the parameter ($s_6 = 0.6$) determined for the PBE0 functional was employed for the HSE06 calculations. Successful tests of these methods on extended crystalline systems are given in refs 62–64.

2.2.2. Periodic Calculations. For all periodic geometries, the nuclear positions, lattice parameters, and cell volumes of the structures were optimized in the ferromagnetic (FM) spin state, which corresponds to ferromagnetic coupling both along a chain of Fe centers and between the chains. These calculations employed a rhombohedral primitive cell (space group $R\bar{3}$, Figure 1) containing 54, 60, and 66 atoms for $\text{Fe}_2(\text{dobdc})$, $\text{Fe}_2(\text{O})_2(\text{dobdc})$, and $\text{Fe}_2(\text{OH})_2(\text{dobdc})$, respectively.

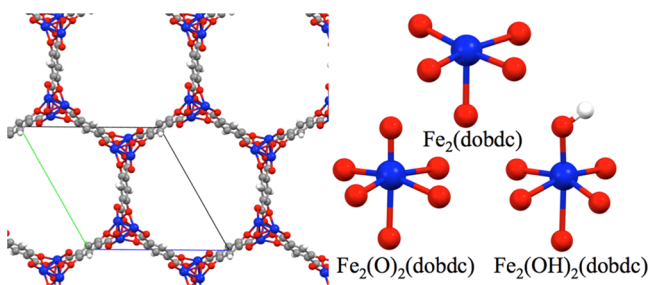


Figure 1. (Left) Primitive unit cell^{67,68} of $\text{Fe}_2(\text{dobdc})$; the figure also shows nearby atoms from other cells. (Right) First coordination sphere of the metal centers within the three MOFs studied. (Atom legend: blue = Fe, red = O, gray = C, and white = H.)

In these calculations, projector-augmented wave^{65,66} (PAW) potentials were used to describe the interaction between explicitly treated electrons and the electrons treated as core electrons, namely, the inner 10 electrons of each Fe center. Two partial waves were used for each orbital: a cutoff radius of 2.0 bohrs (a_0) was used for the $3p$ and $4s$ states, and a cutoff radius of $2.2 a_0$ was used for the $3d$ states.

Because of the relatively small band gap and weak long-range magnetic interactions reported for $\text{Fe}_2(\text{dobdc})$,¹⁴ it is especially important to converge the MOF structures and energies, with respect to the number of k -points used for quadratures over the Brillouin zone.

Our convergence tests and final choices of grids are summarized in the Supporting Information (SI).

Density functional perturbation theory (DFPT),^{69–72} also called linear response theory (LRT), was employed to compute the infrared spectra in the harmonic approximation. The PBE+U functional was used to compute all frequencies with an energy convergence threshold of 10^{-6} eV. Only the vibrations of Fe, carboxylate C, and O atoms were included in the DFPT calculation. The vibrational eigenmodes of each species were determined by the direct force constant approach.⁷¹ The intensities of the infrared active modes were calculated in the dipole approximation by using Born Effective Charges (BECs).⁶⁹

2.2.3. Cluster Calculations. All cluster calculations were performed using the Gaussian 09⁷³ software package on models similar to those used in previous research.^{15,18} The models contain two or three Fe ions. For the model with two Fe ions, we can compute nearest-neighbor coupling, and for the models with three Fe ions both the nearest-neighbor and the next-nearest-neighbor couplings can be computed (Figure 2). The models with two Fe ions were cut from the

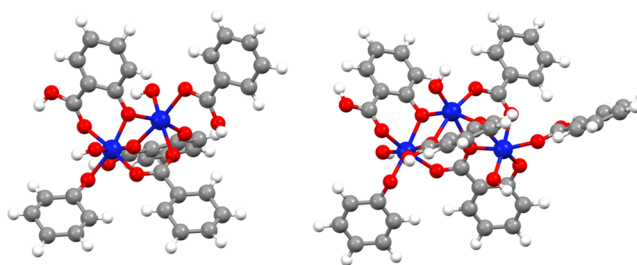


Figure 2. Cluster models with both (left) two Fe ions and (right) three Fe ions used for $\text{Fe}_2(\text{OH})_2(\text{dobdc})$. (Atom legend: blue = Fe, red = O, gray = C, and white = H.)

experimental structure of $\text{Fe}_2(\text{dobdc})$, and the models with three Fe ions were cut from the periodically optimized PBE+U structures of each of the three MOFs. The cut bonds were then capped with H atoms. In the two-Fe model, the $\text{Fe}\cdots\text{Fe}$ distance and $\text{Fe}-\text{O}_c-\text{Fe}$ angle (shown later in this work in Figure 5) were frozen to certain values, and the rest of the cluster was optimized using M06-L/def2-TZVP. This was followed by M06//M06-L single-point calculations with ferromagnetic and antiferromagnetic ordering to extract the nearest-neighbor magnetic coupling constant. In the models with three Fe ions, the hydrogen positions were optimized with M06-L³³ and the def2-SV(P)⁷⁴ basis set. Single-point calculations were then performed with ferromagnetic and antiferromagnetic ordering using the def2-TZVP⁷⁴ basis set and the PBE,³⁰ PBE0,^{48,49} M06,⁵⁰ HSE06,^{53,57–59} and B3LYP^{44–47} exchange–correlation functionals.

2.2.4. Magnetic Coupling Parameters. Previous work has demonstrated that the Fe centers in each of the species have high-spin ground states; namely, $\text{Fe}_2(\text{dobdc})$ contains quintet Fe(II) centers, $\text{Fe}_2(\text{O})_2(\text{dobdc})$ contains quintet Fe(IV) centers, and $\text{Fe}_2(\text{OH})_2(\text{dobdc})$ contains sextet Fe(III) centers.^{9,14,16,19,20} Hence, only high-spin metal centers were considered in the magnetic coupling calculations. The periodic DFT calculations for $\text{Fe}_2(\text{dobdc})$, $\text{Fe}_2(\text{O})_2(\text{dobdc})$, and $\text{Fe}_2(\text{OH})_2(\text{dobdc})$ were performed with the unit cells specified above^{67,68} (Figure 1). The PBE, PBE+U, PBE+U-D2, HSE06, HSE06-D2, and GAM+U geometries were each fixed to those optimized for the FM spin state, and the plane-wave coefficients were optimized for each of the three spin configurations shown in Figure 3 with an energy convergence threshold of 10^{-6} eV.

The unit cell used in this study contains two vertices of one of the hexagonal channels of $\text{Fe}_2(\text{dobdc})$ shown in Figure 1 with three Fe ions in each of the two vertices. The considered spin alignments of the six high-spin Fe ions are provided in Figure 3. The broken symmetry approximation²⁶ allowed us to use the energy differences between these three spin configurations to compute the nearest-neighbor (J_{NN}) and interchain (J_{IC}) coupling values with the Heisenberg–Dirac–Van Vleck (HDV) Hamiltonian:^{75–77}

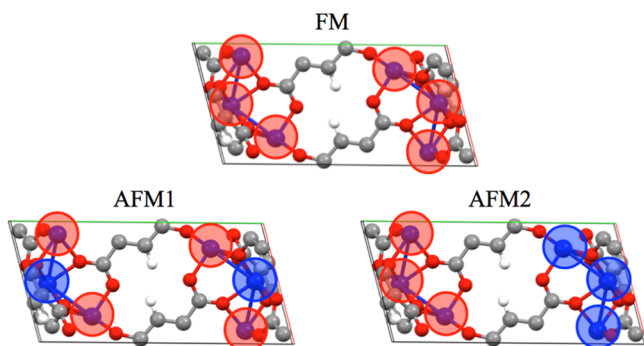


Figure 3. Side view of the primitive unit cell of $\text{Fe}_2(\text{dobdc})$ (atom legend: blue = Fe, red = O, gray = C, and white = H). Red and blue circles indicate the upward or downward spin of the high-spin Fe ions, respectively. The entirely ferromagnetic (FM), intrachain antiferromagnetic (AFM1), and interchain antiferromagnetic (AFM2) spin states were considered in this work. AFM1 is actually ferrimagnetic with this unit cell. Results with a doubled unit cell with strict intrachain AFM coupling are provided in the Supporting Information (SI).

$$H_{\text{HDV}} = -2 \sum_{j>i} \sum_i J_{ij} \hat{S}_i \cdot \hat{S}_j \quad (1)$$

where the subscripts i and j represent the Fe sites of the unit cell shown in Figure 4, J_{ij} is the isotropic magnetic coupling between

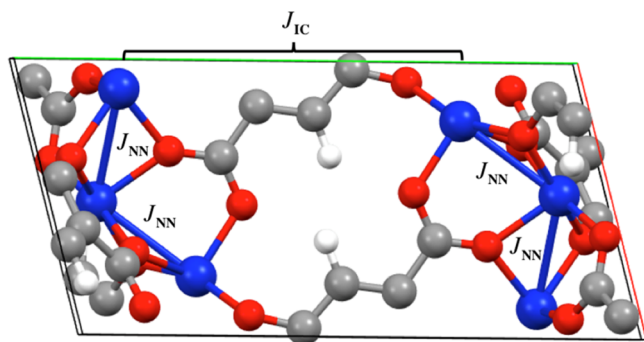


Figure 4. Schematic representation of the nearest-neighbor coupling constant (J_{NN}) and the interchain coupling constant (J_{IC}) of the primitive unit cell of $\text{Fe}_2(\text{dobdc})$. (Atom legend: blue = Fe, red = O, gray = C, and white = H.)

magnetic sites i and j , and \hat{S}_i is the spin vector on center i . A positive J_{ij} in eq 1 denotes ferromagnetic (FM) coupling between centers i and j , and a negative value indicates antiferromagnetic (AFM) coupling. Note that only matrix elements that contain high-spin Fe sites (i.e., diagonal matrix elements) are eigenfunctions of the HDV Hamiltonian. Also note that the diagonal matrix elements in the HDV Hamiltonian are equivalent to those of the Ising model, which is commonly used for magnetic systems.^{9,78} We considered one FM state and two AFM states (AFM1 and AFM2) to be the ones that allow the most direct calculation of the magnetic couplings; note that AFM2 is the ground-state configuration of $\text{Fe}_2(\text{dobdc})$.

Since all Fe sites in $\text{Fe}_2(\text{dobdc})$ and its derivatives $\text{Fe}_2(\text{O})_2(\text{dobdc})$ and $\text{Fe}_2(\text{OH})_2(\text{dobdc})$ are equivalent, the four nearest-neighbor interactions represented by J_{NN} in Figure 4 are all equivalent. For the atoms at the edge of the unit cell, additional nearest-neighbor interactions arise due to interaction with the periodic image of the unit cell. This accounts for two more J_{NN} values, resulting in a total of six J_{NN} for the primitive cell.

While the treatment described above for nearest-neighbor interactions is unambiguous, the treatment of interchain coupling requires more consideration. Each chain of Fe ions is surrounded by three other chains of Fe ions. Although the three neighboring chains

are equally distant, the Fe ions are staggered, so that the smallest interchain Fe...Fe distance is not the same for all three neighboring chains of a given Fe ion; in particular, the distance to the nearest Fe ion in each of the three surrounding chains in $\text{Fe}_2(\text{dobdc})$ is 7.4, 8.1, and 9.0 Å. If the data were sufficient to accommodate a multi-parameter analysis, one would recognize at least three different interchain couplings and also include next-nearest neighbors within a given chain. However, the interchain coupling was found to be small, and the theory might not be good enough to distinguish several different small couplings. Even more significantly, the experiment (as explained in section 2.1) was interpreted in terms of only two parameters, one intrachain parameter J_{NN} and one interchain parameter zJ_{IC} . Therefore, we took the same approach computationally. However, we obtained slightly different results if we assumed that the interchain coupling was caused only by the nearest interchain interaction ($z = 1$) or was caused by equal interactions with the nearest neighbors in each of the three surrounding chains ($z = 3$). We will report the equations and the resulting magnetic coupling for the approach in which we computed the magnetic coupling values, assuming that each metal center would interact with only the closest metal center of the three neighboring chains, which was reasonable, because one of the interchain Fe...Fe distances was smaller than the other two. This limited interchain coupling model, corresponding to $z = 1$, leads to a total of six interactions per unit cell. The model with $z = 3$ would lead to 18. We note that the two treatments yield identical values of zJ_{IC} but slightly different values of J_{NN} (Table S5).

Using the energies calculated for the three spin states (FM, AFM1, and AFM2) shown in Figure 3, the J_{NN} and J_{IC} values can be extracted for $\text{Fe}_2(\text{dobdc})$ and $\text{Fe}_2(\text{O})_2(\text{dobdc})$ (which have total spin magnitudes ($|M_S|$) of 2 on every Fe site) by solving the following three equations:

$$\begin{aligned} \langle 222, 222 | H_{\text{HDV}} | 222, 222 \rangle &= E_{222,222} = -2[6J_{\text{NN}} \cdot 2 \cdot 2 + 6J_{\text{IC}} \cdot 2 \cdot 2] \\ \langle \bar{2}\bar{2}\bar{2}, \bar{2}\bar{2}\bar{2} | H_{\text{HDV}} | \bar{2}\bar{2}\bar{2}, \bar{2}\bar{2}\bar{2} \rangle &= E_{\bar{2}\bar{2}\bar{2},\bar{2}\bar{2}\bar{2}} = -2[-2J_{\text{NN}} \cdot 2 \cdot 2 + 6J_{\text{IC}} \cdot 2 \cdot 2] \\ \langle 222, \bar{2}\bar{2}\bar{2} | H_{\text{HDV}} | 222, \bar{2}\bar{2}\bar{2} \rangle &= E_{222,\bar{2}\bar{2}\bar{2}} = -2[6J_{\text{NN}} \cdot 2 \cdot 2 - 6J_{\text{IC}} \cdot 2 \cdot 2] \end{aligned} \quad (2)$$

where H_{HDV} is the HDV Hamiltonian of eq 2, $|222, 222\rangle$ and $E_{222,222}$ represent the Slater determinant and total energy of the FM case (Figure 3), $|\bar{2}\bar{2}\bar{2}, \bar{2}\bar{2}\bar{2}\rangle$ and $E_{\bar{2}\bar{2}\bar{2},\bar{2}\bar{2}\bar{2}}$ represent the Slater determinant and total energy of the AFM1 case, and $|222, \bar{2}\bar{2}\bar{2}\rangle$ and $E_{222,\bar{2}\bar{2}\bar{2}}$ represent the Slater determinant and total energy of the AFM2 case. In the Slater determinants of eq 2, the M_S values before the comma are the values for one chain containing three Fe centers and the ones after the comma are for the other chain. Solving the equations given by eq 2 results in the values of J_{NN} and J_{IC} which are represented by the following equations:

$$\begin{aligned} J_{\text{IC}} &= \frac{1}{96} [E_{222,\bar{2}\bar{2}\bar{2}} - E_{222,222}] \\ J_{\text{NN}} &= \frac{1}{64} [E_{\bar{2}\bar{2}\bar{2},\bar{2}\bar{2}\bar{2}} - E_{222,222}] \end{aligned} \quad (3)$$

For the unit cell of $\text{Fe}_2(\text{OH})_2(\text{dobdc})$, where each Fe ion has a spin of $S/2$, the J_{NN} and J_{IC} values can be extracted by solving the following three equations:

$$\begin{aligned}
 \left\langle \frac{\bar{S} \bar{S} \bar{S}}{2 \ 2 \ 2}, \frac{\bar{S} \bar{S} \bar{S}}{2 \ 2 \ 2} | H_{\text{HDV}} | \frac{\bar{S} \bar{S} \bar{S}}{2 \ 2 \ 2}, \frac{\bar{S} \bar{S} \bar{S}}{2 \ 2 \ 2} \right\rangle &= E_{\frac{\bar{S} \bar{S} \bar{S}}{2 \ 2 \ 2}, \frac{\bar{S} \bar{S} \bar{S}}{2 \ 2 \ 2}} \\
 &= -2 \left[6J_{\text{NN}} \frac{\bar{S}}{2} \cdot \frac{\bar{S}}{2} + 6J_{\text{IC}} \frac{\bar{S}}{2} \cdot \frac{\bar{S}}{2} \right] \\
 \left\langle \frac{\bar{S} \bar{S} \bar{S}}{2 \ 2 \ 2}, \frac{\bar{S} \bar{S} \bar{S}}{2 \ 2 \ 2} | H_{\text{HDV}} | \frac{\bar{S} \bar{S} \bar{S}}{2 \ 2 \ 2}, \frac{\bar{S} \bar{S} \bar{S}}{2 \ 2 \ 2} \right\rangle &= E_{\frac{\bar{S} \bar{S} \bar{S}}{2 \ 2 \ 2}, \frac{\bar{S} \bar{S} \bar{S}}{2 \ 2 \ 2}} \\
 &= -2 \left[-2J_{\text{NN}} \frac{\bar{S}}{2} \cdot \frac{\bar{S}}{2} + 6J_{\text{IC}} \frac{\bar{S}}{2} \cdot \frac{\bar{S}}{2} \right] \\
 \left\langle \frac{\bar{S} \bar{S} \bar{S}}{2 \ 2 \ 2}, \frac{\bar{S} \bar{S} \bar{S}}{2 \ 2 \ 2} | H_{\text{HDV}} | \frac{\bar{S} \bar{S} \bar{S}}{2 \ 2 \ 2}, \frac{\bar{S} \bar{S} \bar{S}}{2 \ 2 \ 2} \right\rangle &= E_{\frac{\bar{S} \bar{S} \bar{S}}{2 \ 2 \ 2}, \frac{\bar{S} \bar{S} \bar{S}}{2 \ 2 \ 2}} \\
 &= -2 \left[6J_{\text{NN}} \frac{\bar{S}}{2} \cdot \frac{\bar{S}}{2} - 6J_{\text{IC}} \frac{\bar{S}}{2} \cdot \frac{\bar{S}}{2} \right]
 \end{aligned} \tag{4}$$

The only difference between the equations for the $\text{Fe}_2(\text{dobdc})$ and $\text{Fe}_2(\text{O})_2(\text{dobdc})$ cases and the $\text{Fe}_2(\text{OH})_2(\text{dobdc})$ case is the spin (M_S) of the Fe ions. This change results in different prefactors for the J_{NN} and J_{IC} magnetic coupling values. Solving the relationships described in eq 4 gives the values of J_{NN} and J_{IC} for $\text{Fe}_2(\text{OH})_2(\text{dobdc})$, which are represented by eq 5:

$$\begin{aligned}
 J_{\text{IC}} &= \frac{1}{150} \left[E_{\frac{\bar{S} \bar{S} \bar{S}}{2 \ 2 \ 2}, \frac{\bar{S} \bar{S} \bar{S}}{2 \ 2 \ 2}} - E_{\frac{\bar{S} \bar{S} \bar{S}}{2 \ 2 \ 2}, \frac{\bar{S} \bar{S} \bar{S}}{2 \ 2 \ 2}} \right] \\
 J_{\text{NN}} &= \frac{1}{100} \left[E_{\frac{\bar{S} \bar{S} \bar{S}}{2 \ 2 \ 2}, \frac{\bar{S} \bar{S} \bar{S}}{2 \ 2 \ 2}} - E_{\frac{\bar{S} \bar{S} \bar{S}}{2 \ 2 \ 2}, \frac{\bar{S} \bar{S} \bar{S}}{2 \ 2 \ 2}} \right]
 \end{aligned} \tag{5}$$

Additional considerations in the above two-parameter treatment are the neglect of next-nearest-neighbor interactions in a given chain and the fact that the periodically replicated AFM1 state is not strictly antiferromagnetic down each chain of metals. A more faithful representation of a fully antiferromagnetic chain can be obtained by doubling the size of the primitive cell along the c -axis (which runs parallel to the chains) from 54 atoms to 108 atoms for $\text{Fe}_2(\text{dobdc})$ (Figure S15), from 60 atoms to 120 atoms for $\text{Fe}_2(\text{O})_2(\text{dobdc})$, and from 66 atoms to 132 atoms for $\text{Fe}_2(\text{OH})_2(\text{dobdc})$. Single-point calculations were performed on the doubled unit cells with PBE+U to test the validity of utilizing the smaller cells shown in Figures 3 and 4. We also computed the J_{NN} and J_{NNN} magnetic couplings with cluster models. For the cluster calculations, the Hamiltonian and equations used to compute the magnetic coupling values with the cluster models are described in the SI along with coordinates for each cluster model.

3. RESULTS AND DISCUSSION

3.1. Equilibrium Structures and Infrared Spectra. The SI compares equilibrium structures computed by PBE, PBE+U, PBE+U-D2, HSE06, HSE06-D2, and GAM+U. In the case of $\text{Fe}_2(\text{dobdc})$, there is good agreement between the bond distances and angles computed with all the methods and the experiment, with the exception of PBE, which significantly underestimates the $\text{Fe}\cdots\text{Fe}$ distances and the $\text{Fe}-\text{O}_c-\text{Fe}$ angle. Table S2 in the SI shows that, after oxidation to Fe(III), the experimental $\text{Fe}\cdots\text{Fe}$ distance increases by 0.15–0.16 Å. If we ignore PBE, because of its underestimation of the $\text{Fe}\cdots\text{Fe}$ distance in $\text{Fe}_2(\text{dobdc})$, the density functional calculations predict that there is an increase in the $\text{Fe}\cdots\text{Fe}$ distance by 0.25–0.28 Å. Figure 5 shows the local environment of a metal center in $\text{Fe}_2(\text{OH})_2(\text{dobdc})$ and the organic linker.

The experimental infrared (IR) spectra of $\text{Fe}_2(\text{dobdc})$ and $\text{Fe}_2(\text{OH})_2(\text{dobdc})$ in Figure 6 provide a good test of the PBE+U computations, which are depicted in Figure 7. The theoretical spectra were normalized to match the intensities of the experimental Fe–O stretches that occur at $\sim 820 \text{ cm}^{-1}$. The peaks occurring below 500 cm^{-1} are likely due to Fe–O bending modes, while those between 600 and 1000 cm^{-1} are due to Fe–O stretches. The PBE+U Fe(III)–OH stretching

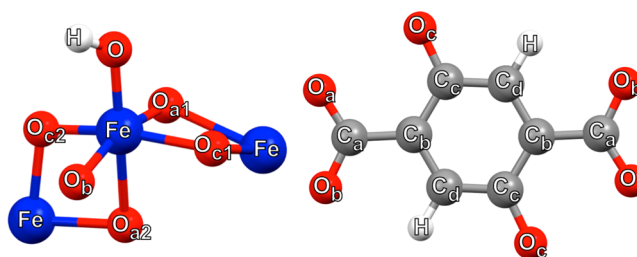


Figure 5. (left) The first coordination sphere of the metal center in $\text{Fe}_2(\text{OH})_2(\text{dobdc})$ and (right) the organic linker. The four unique oxygens, four unique carbons, and two unique hydrogens are shown. Note that the O_{a1} , O_{a2} , O_{c1} , and O_{c2} labeling used here and in Table S2 distinguish the Fe–O bond positions, with respect to the central Fe. The $\text{Fe}-\text{O}_{a1}-\text{Fe}$ and $\text{Fe}-\text{O}_{a2}-\text{Fe}$ bond angles, as well as the $\text{Fe}-\text{O}_{c1}-\text{Fe}$ and $\text{Fe}-\text{O}_{c2}-\text{Fe}$ bond angles, are equivalent. (Atom legend: blue = Fe, red = O, gray = C, and white = H.)

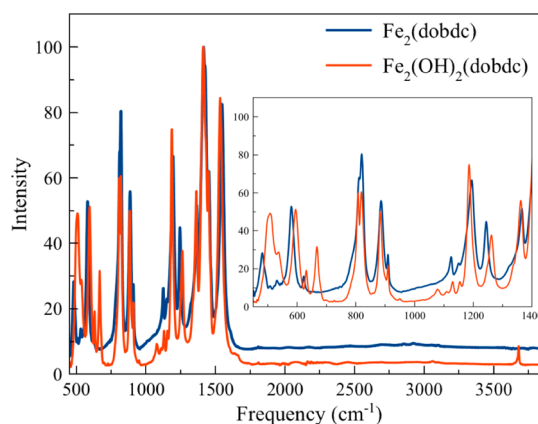


Figure 6. Experimental infrared spectra of $\text{Fe}_2(\text{dobdc})$ and $\text{Fe}_2(\text{OH})_2(\text{dobdc})$ (see ref 19).

frequencies in $\text{Fe}_2(\text{OH})_2(\text{dobdc})$ occur between 619 and 630 cm^{-1} , which is $\sim 40 \text{ cm}^{-1}$ less than the experimental value of 667 cm^{-1} .¹⁹

The PBE+U O–H stretching frequency in $\text{Fe}_2(\text{OH})_2(\text{dobdc})$ is 3773 cm^{-1} , and the experimental value is 3683 cm^{-1} . The Fe(IV)–oxo stretch is known, in other cases, to occur between 776 cm^{-1} and 843 cm^{-1} .⁸¹ We find that the PBE+U Fe(IV)–oxo stretches occur here between 888 cm^{-1} and 899 cm^{-1} . Thus, the theory underestimates the Fe(III)–OH stretching frequency and may overestimate the Fe(IV)–oxo stretching frequency. However, the experimental Fe(IV)–oxo-containing material is quite different than the theoretical model. Calculations with the actual experimental composition ($\text{Fe}_{0.1}(\text{O})_{0.1}\text{Mg}_{1.9}(\text{dobdc})$) may yield more accurate frequencies. Molecular DFT calculations are known to systematically overestimate experimental fundamental stretching frequencies, but usually by only 2%–5%.⁸²

3.2. Electronic Structure and Density of States. To gain insight into the electronic structures, the orbital projected density of states (OP-DOS) is provided for each MOF in the SI. The OP-DOS plots were extracted using the default settings for atomic radii in VASP. The atomic radii could be considered tunable parameters that can be improved by computing and comparing to reasonable atomic charges,⁸³ but the default parameters yielded decent results, when compared to the experiment. Figures S3 and S4 show the OP-DOS obtained using PBE+U and HSE06, respectively, for each MOF in its

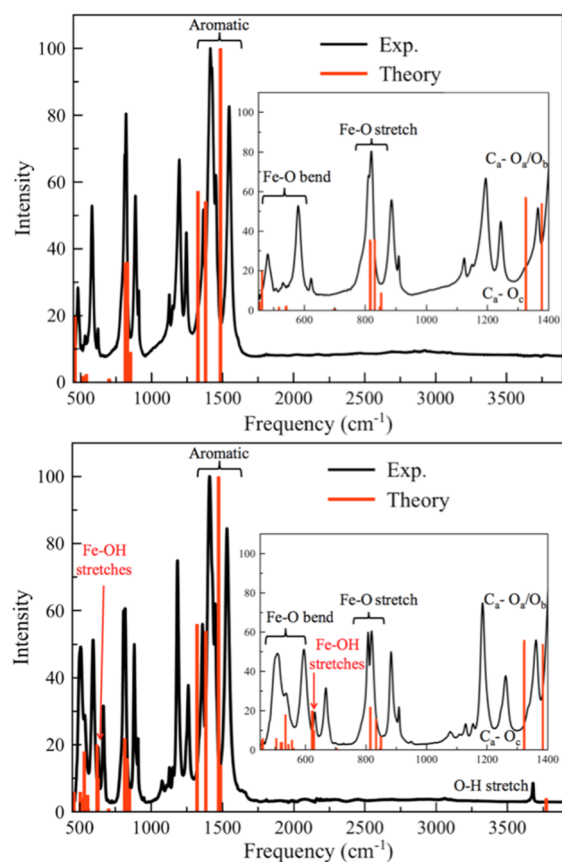


Figure 7. Experimental and theoretical (PBE+U) infrared spectra of (top) $\text{Fe}_2(\text{dobdc})$ and (bottom) $\text{Fe}_2(\text{OH})_2(\text{dobdc})$. All spectra were normalized based on the highest peak. The experimental spectra for $\text{Fe}_2(\text{dobdc})$ were taken from ref 19. The Fe–OH stretch theoretical peak intensities (those that are indicated by the red arrow in the range from 619 cm^{-1} to 630 cm^{-1}) were multiplied by a factor of 10 for more visible comparison to the experiment.

lowest-energy spin state (Table 1). We consider only the projections of the DOS on the Fe $3d$ and O $2p$ orbitals, since the electrons occupying these orbitals are the ones mainly responsible for the magnetic properties. To identify the bands of the “additional” O atoms in $\text{Fe}_2(\text{O})_2(\text{dobdc})$ and $\text{Fe}_2(\text{OH})_2(\text{dobdc})$, the figures also show projections that include only the $2p$ orbitals of the added O atoms.

The main consideration in these plots is the band gap, i.e., the difference in energy between the highest occupied orbital and the lowest unoccupied one. PBE+U and HSE06 both predict a sizable band gap, in particular 1.3 and 2.1 eV, respectively, which are substantially larger than the gap of 0.3 eV reported by Zhang et al. ref 14). We investigated the reason for this discrepancy and found that the band gap decreased as the volume increased, but even with a 15% volume fluctuation, the band gap remained between 1.1 eV and 0.8 eV. Furthermore, a single-point calculation with the experimental structure gives the same band gap as that obtained from the equilibrium PBE+U structure determined in this work. The trend in the gap upon increasing the oxidation state of iron is different for PBE+U and HSE06. The PBE+U gaps for the Fe(IV) and Fe(III) MOFs are almost identical (0.8 eV), while HSE06 predicts a gap of 1.5 eV for $\text{Fe}_2(\text{O})_2(\text{dobdc})$, which contains Fe(IV), but predicts a larger gap of 1.8 eV for $\text{Fe}_2(\text{OH})_2(\text{dobdc})$, which contains Fe(III).

3.3. Magnetic Susceptibility Measurements. The magnetic susceptibility of $\text{Fe}(\text{II})_{0.26}[\text{Fe}(\text{III})(\text{OH})]_{1.74}(\text{dobdc})(\text{DMF})_{0.15}(\text{THF})_{0.22}$ (“ $\text{Fe}_2(\text{OH})_2(\text{dobdc})$ ”) was measured in the present work. DC magnetic susceptibility measurements were performed under an applied magnetic field of 1000 Oe across the temperature range of 2–300 K. The measurements of $\text{Fe}_2(\text{OH})_2(\text{dobdc})$ revealed a decreasing $\chi_M T$ product with decreasing temperature across the full temperature range measured (Figure 8). This trend supports the assignment of

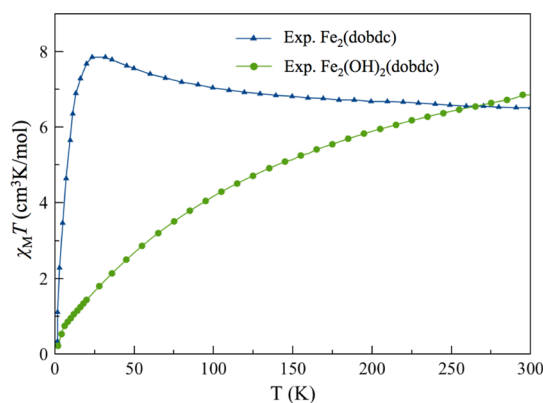


Figure 8. Experimental magnetic susceptibility times temperature curves of $\text{Fe}_2(\text{dobdc})$ ¹⁶ (blue) and $\text{Fe}_2(\text{OH})_2(\text{dobdc})$ (green). The applied magnetic field strength during the susceptibility measurement of each material was 1000 Oe.

both intrachain and interchain magnetic couplings as antiferromagnetic. The $\chi_M T$ value at 300 K and 1000 Oe is 6.85 emu K/mol, which is much lower than both the expected value for two isotropic $S = 5/2$ spins (8.75 emu K/mol) and the expected value assuming 0.26 mol (13% of iron sites) of $S = 2$ Fe(II) per formula unit (8.39 emu K/mol). The low magnetic moment is attributed to the presence of 13% Fe(II), which, in addition to simply having a lower magnetic moment than that of Fe(III), may also display enhanced antiferromagnetic coupling with its nearest-neighbor spins. The magnetic susceptibility of $\text{Fe}_2(\text{dobdc})$ was measured in ref 16, where the fitting procedure used to compute the experimental coupling values for $\text{Fe}_2(\text{dobdc})$ is also described. The fitting procedure is briefly summarized in section 2.1.

It was not feasible to extract the interchain and intrachain magnetic coupling parameters with the Fisher model, as was done for $\text{Fe}_2(\text{dobdc})$.¹⁶ The results in Figure 8 indicate that $\text{Fe}_2(\text{dobdc})$ has ferromagnetic intrachain coupling and antiferromagnetic interchain coupling. The precise coupling parameters for $\text{Fe}_2(\text{OH})_2(\text{dobdc})$ could not be readily derived because of the fact that the synthesized MOF was only partially oxidized, with $\sim 13\%$ of the Fe sites remaining in the Fe(II) state. However, a Curie–Weiss fit to the expression $1/\chi_M = (T - \theta)/C$ for the high-temperature regime (50–300 K) of the inverse magnetic susceptibility data for both $\text{Fe}_2(\text{dobdc})$ and $\text{Fe}_2(\text{OH})_2(\text{dobdc})$ (Figure S18) permitted some assessment of the differences in magnetic coupling behaviors for the two frameworks. For $\text{Fe}_2(\text{dobdc})$, the Curie–Weiss analysis resulted in a positive Weiss temperature of $\theta = 11\text{ K}$, which is consistent with ferromagnetic interactions being dominant, and a Curie constant of $C = 6.3\text{ emu K/mol}$. In contrast, the Curie–Weiss analysis for $\text{Fe}_2(\text{OH})_2(\text{dobdc})$ resulted in $\theta = -139\text{ K}$ and $C = 10.0\text{ emu K/mol}$. The negative sign of the Weiss temperature (θ) for $\text{Fe}_2(\text{OH})_2(\text{dobdc})$ indicates that antiferromagnetic

Table 1. Periodic DFT Exchange and Coupling Energies of the Fe Centers^a

method	number of atoms	$E_{AFM1} - E_{FM}^b$ (cm ⁻¹)	$E_{AFM2} - E_{FM}$ (cm ⁻¹)	J_{NN}^c (cm ⁻¹)	zJ_{IC}
Fe(II) Case: Fe ₂ (dobdc)					
PBE	54	7287.7	-160.0	113.9	-5.0
PBE+U ^d	108	56.6 (92.9)	-121.1	0.5 (0.3)	-1.9
PBE+U	54	41.6	-60.4	0.7	-1.9
PBE+U-D2	54	31.1	-64.6	0.5	-2.0
HSE06	54	171.6	-32.2	2.7	-1.0
HSE06-D2	54	163.2	-47.5	2.6	-1.5
GAM+U	54	145.4	-52.8	2.3	-1.7
expt ^e				4.1	-1.1
Fe(III) Case: Fe ₂ (OH) ₂ (dobdc)					
PBE	66	-2308.1	-2042.3	-23.1	-40.8
PBE+U ^d	132	-3216.0 (-2259.0)	-630.7	-10.2 (-1.1)	-6.3
PBE+U	66	-1129.6	-315.9	-11.3	-6.3
PBE+U-D2	66	-1133.9	-311.7	-11.3	-6.2
HSE06	66	-562.0	-169.8	-5.6	-3.4
HSE06-D2	66	-561.4	-170.3	-5.6	-3.4
GAM+U	66	-691.7	-272.7	-6.9	-5.5
Fe(IV) Case: Fe ₂ (O) ₂ (dobdc)					
PBE	60	-795.8	-164.1	-12.4	-5.1
PBE+U ^d	120	-205.6 (-270.2)	81.1	-1.2 (-0.9)	1.3
PBE+U	60	-133.8	40.9	-2.1	1.3
PBE+U-D2	60	-157.6	36.1	-2.5	1.1
HSE06	60	-31.8	17.9	-0.5	0.6
HSE06-D2	60	-43.3	15.8	-0.7	0.5
GAM+U	60	17.5	-42.4	0.3	-1.3

^aAll coupling values were extracted using geometries optimized with the FM spin state. E_{FM} is the electronic energy of the ferromagnetic state, E_{AFM1} is the electronic energy of antiferromagnetic state 1, and E_{AFM2} is the electronic energy of antiferromagnetic state 2 (Figure 3). E_{AFM3} is the electronic energy of antiferromagnetic state 3 of the supercell. J_{NN} , J_{IC} and J_{NNN} coupling parameters represent the nearest-neighbor, interchain, and next-nearest-neighbor magnetic couplings, respectively (Figure 4). ^bValues shown in parentheses represent the value of $E_{AFM3} - E_{FM}$ (cm⁻¹). ^cValues shown in parentheses represent the J_{NNN} value (cm⁻¹). ^dThe equations used to calculate the coupling parameters for the doubled cells are in the SI; the spin configurations for the doubled cells are shown in Figure S17 in the SI. ^eData taken from ref 16.

interactions are prevalent. Concurrently, the large increase in the magnitude of θ , which is dependent on the spin states present and the number and strength of the magnetic coupling pathways,⁸⁴ suggests that the magnetic interactions are stronger within Fe₂(OH)₂(dobdc), since the Fe spins involved only increase from quintet to sextet states, while the number of magnetic coupling pathways presumably remains unchanged. Thus, we can state qualitatively that adding a hydroxide anion and oxidizing the metal sites of Fe₂(dobdc) switches the nearest-neighbor magnetic coupling behavior from ferromagnetic to antiferromagnetic and increases the magnetic coupling strength.

3.4. Magnetic Coupling Parameters. The calculated magnetic coupling parameters for Fe₂(dobdc), Fe₂(O)₂(dobdc), and Fe₂(OH)₂(dobdc) are provided in Tables 1 and 2. As mentioned above, the PBE+U calculations were run with both primitive unit cells (54, 60, or 66 atoms) and doubled cells (108, 120, or 132 atoms), as indicated in the second column of Table 1. This table shows that there is no significant difference between the PBE+U calculations with 54 and 108 atoms in the unit cell, which indicates that the primitive cell is adequate for these computations. The same is true for couplings in Fe₂(O)₂(dobdc) and Fe₂(OH)₂(dobdc).

The PBE nearest-neighbor couplings in Fe₂(dobdc) are two orders of magnitude larger than both the experimental ones and those computed with the other methods tested in Table 1. The PBE values are calculated for the PBE geometry, which has short Fe...Fe distances. The overestimation of magnetic

properties by GGA functionals is well-established.⁸⁵ A previous study⁹ of magnetic interactions in Fe₂(dobdc) employed the PBE exchange-correlation functional with experimental geometries and obtained a J_{NN} value of 28 cm⁻¹, which is smaller but still a significant overestimation. They concluded⁹ that there is fairly strong ferromagnetic coupling in Fe₂(dobdc). It now appears that such large calculated J_{NN} values are an artifact of the simple gradient approximation used in the PBE functional. This was shown in previous work,¹⁸ where a calculation with a hybrid meta-GGA gave a value of 3.6 cm⁻¹, in good agreement with the experimental value of 4.1 cm⁻¹.

It was pointed out in section 2.2.4 that the magnetic coupling constants are slightly dependent on whether we perform the analysis with $z = 1$ or $z = 3$. The nearest-neighbor Fe...Fe distance is 3.0 Å, and the next-nearest neighbor Fe...Fe distance within a chain is 5.0 Å. Thus, the next-nearest-neighbor distance is significantly shorter than the shortest interchain Fe...Fe separation, which suggests that the next-nearest-neighbor intrachain coupling should be calculated. The next-nearest-neighbor coupling results are shown in Table 1, where we report the results with $z = 1$. (Note that the value computed for J_{IC} is independent of whether or not J_{NNN} is computed and is also independent of whether we use $z = 1$ or $z = 3$.) Excluding PBE, the nearest-neighbor couplings (J_{NN}) obtained with $z = 3$ are very similar for Fe₂(dobdc), Fe₂(OH)₂(dobdc), and Fe₂(O)₂(dobdc), whereas the results for zJ_{IC} are unchanged. Table 1 shows that the PBE+U and HSE06 calculated values of J_{NN} are smaller than the PBE value and are in more reasonable

agreement with the experiment. For $\text{Fe}_2(\text{dobdc})$, the coupling values obtained by HSE06 and HSE06-D2 are similar to each other and are larger than those predicted by PBE+U, whereas for the $\text{Fe}_2(\text{O})_2(\text{dobdc})$ and $\text{Fe}_2(\text{OH})_2(\text{dobdc})$ cases, HSE06 and HSE06-D2 yield magnetic couplings that are smaller than the values computed with PBE+U and PBE. PBE+U and HSE06 predict the same signs of the magnetic couplings.

Table 1 shows that the periodic calculations of J_{NNN} using PBE+U yield values of 0.3, -1.1 , and -0.9 cm^{-1} for $\text{Fe}_2(\text{dobdc})$, $\text{Fe}_2(\text{OH})_2(\text{dobdc})$, and $\text{Fe}_2(\text{O})_2(\text{dobdc})$, respectively. These J_{NNN} values may be compared to the respective J_{IC} coupling values of -0.6 , -2.1 , and 0.4 cm^{-1} . The magnitude of the PBE+U J_{IC} coupling values for $\text{Fe}_2(\text{dobdc})$ and $\text{Fe}_2(\text{OH})_2(\text{dobdc})$ are larger than the J_{NNN} values, while the PBE+U J_{IC} value of $\text{Fe}_2(\text{O})_2(\text{dobdc})$ is smaller than the J_{NNN} value. Note that the J_{IC} coupling values for $\text{Fe}_2(\text{OH})_2(\text{dobdc})$ are notably larger than the other two cases with all functionals. This may indicate that, separate from the oxidation of the metal centers, addition of the $(\text{OH})^-$ groups enhances interchain magnetic coupling.

Table 2 provides the results of cluster model calculations that may be compared to the periodic calculations in Table 1.

Table 2. Isotropic Magnetic Coupling Constants of the Fe Centers for Each Studied MOF, As Obtained by Cluster Calculations^a

method	$J_{\text{NN}}^b \text{ (cm}^{-1}\text{)}$		
	$\text{Fe}_2(\text{dobdc})$	$\text{Fe}_2(\text{OH})_2(\text{dobdc})$	$\text{Fe}_2(\text{O})_2(\text{dobdc})$
PBE//PBE	64.6	-18.2	-9.9
PBE//PBE+U	14.3	-18.7	-9.0
HSE06//PBE+U	2.4 (0.4)	-3.2 (-0.1)	0.3 (-0.2)
M06//PBE+U	4.3	-3.9	-0.5
PBE0//PBE+U	2.5	-3.1	-0.1
B3LYP//PBE+U	2.7	-4.1	-0.5
expt ^c	4.1		

^aX/Y indicates a cluster calculation with method X employing a fragment of a MOF optimized by periodic calculations with method Y. Only nearest- and next-nearest-neighbor intrachain coupling values (J_{NN} and J_{NNN}) were computed, and they may be compared with Table 1. ^bValues shown in parentheses represent the J_{NNN} value (in cm^{-1}). ^cData taken from ref 16.

Because they are very similar to the experimental geometries (Table S2), the PBE+U optimized periodic structures were used to make the clusters in all cases except one. The PBE//PBE J_{NN} value is much larger than the PBE//PBE+U value, in part because the periodic PBE metal–metal bond distances are too small for $\text{Fe}_2(\text{dobdc})$ (as noted above in the discussion of Table S2). The PBE//PBE cluster calculation predicts J_{NN} values for $\text{Fe}_2(\text{dobdc})$ that are significantly larger than experiment. However, the cluster J_{NN} values obtained by HSE06, M06, PBE0, and B3LYP are all quite reasonable, when compared to both the periodic and experimental magnetic coupling parameters.

The results with PBE+U structures in Table 2 show that Hartree–Fock exchange in HSE06, PBE0, M06, and B3LYP decreases the predicted intrachain coupling values. If one assumes that one effect of the U parameter is to mimic Hartree–Fock exchange, this is consistent with the periodic results.

The cluster values of J_{NNN} in Table 2 are considerably smaller than the periodic calculations of J_{NNN} in Table 1. However, they

do correctly predict the experimentally determined magnetic ordering of $\text{Fe}_2(\text{dobdc})$ and $\text{Fe}_2(\text{OH})_2(\text{dobdc})$. In the case of $\text{Fe}_2(\text{O})_2(\text{dobdc})$, the magnetic coupling values are likely extremely weak, which is why GAM+U and HSE06//PBE+U in Table 2 predict different magnetic orderings than the other functionals. This demonstrates the difficulty of accurately calculating the small energies of these interactions.

It was suggested by Park et al.¹⁷ that the changes in magnetism within $\text{Fe}_2(\text{dobdc})$ upon guest adsorption are due to structural changes within the MOF. When the intrachain $\text{Fe}\cdots\text{Fe}$ distances were less than $\sim 3.12 \text{ \AA}$, the magnetic interactions were interpreted as being dominated by direct exchange between the metal centers and were ferromagnetic; at longer $\text{Fe}\cdots\text{Fe}$ separations, the magnetic interactions were interpreted as dominated by superexchange through the bridging O atoms. In our work, $\text{Fe}_2(\text{O})_2(\text{dobdc})$ has intrachain $\text{Fe}\cdots\text{Fe}$ distances of $\sim 3.12 \text{ \AA}$ (Table S2) and the nearest-neighbor AFM coupling is calculated to be very weak (Tables 1 and 2). For comparison, $\text{Fe}_2(\text{OH})_2(\text{dobdc})$ has intrachain $\text{Fe}\cdots\text{Fe}$ distances of $\sim 3.22 \text{ \AA}$ and shows a larger AFM coupling. But the $\text{Fe}\cdots\text{Fe}$ separation is not the only geometrical parameter that changes. The $\text{Fe}-\text{O}_c-\text{Fe}$ bond angles increase from $\text{Fe}_2(\text{dobdc})$ to $\text{Fe}_2(\text{O})_2(\text{dobdc})$ to $\text{Fe}_2(\text{OH})_2(\text{dobdc})$ (see Table S2). Table 1 shows that these structural changes are associated with a switch from positive J_{NN} values to negative J_{NN} values—i.e., a switch from FM to AFM coupling of the nearest-neighbor metal centers. However, many factors besides geometry may contribute to the changes in magnetic coupling. These factors include electronic effects resulting from (1) the presence of the $(\text{OH})^-$ and O^{2-} ligands, (2) the change in oxidation state to Fe(III) for $(\text{OH})^-$ and to Fe(IV) for O^{2-} , and (3) the change in spin state of the metal centers from quintet to sextet, resulting from the inclusion of the $(\text{OH})^-$ ligands. The magnetic coupling equations for $\text{Fe}_2(\text{OH})_2(\text{dobdc})$ (eq 5) take into account the effect of the spin state change (3), but completely separating all three of these electronic contributions from the geometric contributions required a separate set of calculations, as discussed in the next two paragraphs.

To compute the aforementioned electronic contributions, two approaches were considered. In the first approach, the three-Fe cluster model of $\text{Fe}_2(\text{OH})_2(\text{dobdc})$ carved from the PBE+U periodic structure was used. The three $(\text{OH})^-$ groups were removed from this cluster, which changed the Fe(III) centers to Fe(II) centers. While keeping the positions of all atoms in the cluster fixed, magnetic coupling constants were calculated using M06/def2-TZVP. This was done to separate the electronic and geometric contributions to the magnetic coupling. The coupling constant of this new cluster (-1.1 cm^{-1}) should be compared to the M06 magnetic coupling results for $\text{Fe}_2(\text{dobdc})$ (4.3 cm^{-1}) and $\text{Fe}_2(\text{OH})_2(\text{dobdc})$ (-3.9 cm^{-1}) in Table 2. We can see that both electronic and geometric effects play important roles in the magnetic couplings studied here.

The second approach was to go in the reverse direction, meaning that we started with the $\text{Fe}_2(\text{dobdc})$ cluster and then added $(\text{OH})^-$ groups. Three $(\text{OH})^-$ groups were added to the cluster model of $\text{Fe}_2(\text{dobdc})$ carved from the PBE+U periodic structure, and only these added groups were optimized using M06/def2-TZVP, while the remainder of the cluster was kept fixed. The oxidation state and spin state of the metal centers were thus the same as for $\text{Fe}_2(\text{OH})_2(\text{dobdc})$, while the metal coordination geometry was the same as in $\text{Fe}_2(\text{dobdc})$. The

magnetic coupling of $\text{Fe}_2(\text{dobdc})$ (4.3 cm^{-1}) (Table 2) changed to 0.2 cm^{-1} when $(\text{OH})^-$ was added, which is an effect of 4.1 cm^{-1} . The value of 0.2 cm^{-1} can be compared to the M06 magnetic coupling result in Table 2 for $\text{Fe}_2(\text{OH})_2(\text{dobdc})$ of -3.9 cm^{-1} , which also has an effect of 4.1 cm^{-1} . This means that the metal oxidation and addition of $(\text{OH})^-$ and the change in geometry had impacts of similar magnitude. These results show that the presence of the $(\text{OH})^-$ groups (1), the change in oxidation state (2), and the change in spin state (3) all contribute considerably to the magnetic ordering of $\text{Fe}_2(\text{OH})_2(\text{dobdc})$. We also found that the geometry has an important effect on the magnetic coupling. To examine the overall effect of the geometry, we examined the OP-DOS results from the periodic calculations of each structure. However, we also wanted to understand how distinct geometrical parameters, such as Fe...Fe distance and Fe–O–Fe angle, contribute to the magnetic coupling. We thus designed cluster models to separate the contributions of these parameters.

The periodic calculations on $\text{Fe}_2(\text{dobdc})$ (Table 1) are in general agreement with previous work.^{9,14,16,18} The results for the hydroxylated case in Table 1 are consistent with the qualitative inference from the experiment in section 3.3 that oxidation of the metal sites of $\text{Fe}_2(\text{dobdc})$ and concurrent addition of hydroxide anions to these sites switches the nearest-neighbor magnetic coupling behavior from ferromagnetic to antiferromagnetic and increases its strength. The interactions between the bridging O atoms and the Fe atoms can strongly influence the type and magnitude of the magnetic exchange within a material.⁷ The OP-DOS calculations of the Fe 3d and the bridging O 2p orbitals show that overlap between these orbitals is larger for $\text{Fe}_2(\text{O})_2(\text{dobdc})$ and $\text{Fe}_2(\text{OH})_2(\text{dobdc})$ than for $\text{Fe}_2(\text{dobdc})$. This may indicate that there is more interaction between the metal electrons through the bridging oxygens in $\text{Fe}_2(\text{O})_2(\text{dobdc})$ and $\text{Fe}_2(\text{OH})_2(\text{dobdc})$. The increasing Fe–O–Fe bond angle leads to an increase in the magnitude of the AFM coupling, because the electrons in the Fe 3d interact more strongly through the bridging oxygen electrons via superexchange (Figure 9). The superexchange interaction was developed into a set of semiempirical rules by

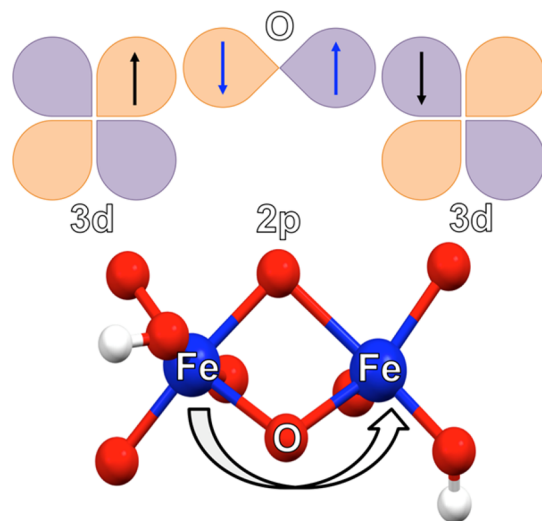


Figure 9. Schematic describing the superexchange interaction that occurs within $\text{Fe}_2(\text{O})_2(\text{dobdc})$ and $\text{Fe}_2(\text{OH})_2(\text{dobdc})$. (Atom legend: blue = Fe atoms, red = O atoms, and white = H atoms.)

Goodenough and Kanamori.⁷ These rules predict an AFM interaction if the metal–ligand–metal angle is close to 180° , and a weak FM interaction if the angle is close to 90° . The computations performed in this work align reasonably well with these rules, although the actual situation is complicated by the fact that the Fe–O distances and Fe...Fe distances change, along with the change in bond angle. Similar interaction trends have been observed previously within $\text{Fe}_2(\text{dobdc})$ when olefins were bound to the metal centers.^{16,17}

In order to somewhat separate changes in intrachain Fe...Fe distances and Fe–O–Fe angles, we performed cluster calculations using the two-Fe model, where two degrees of freedom, Fe...Fe distance and Fe–O_c–Fe angle, were set to (2.9 \AA , 85°), (2.9 \AA , 105°), (3.1 \AA , 95°), (3.3 \AA , 85°), and (3.3 \AA , 105°) to see how the change in either the Fe...Fe distance or the Fe–O–Fe angle affects the magnetic coupling. With these two internal coordinates frozen, all other coordinates were optimized. The J_{NN} values were found to be 10, -6.3 , 1.5, 5.0, and -1.2 cm^{-1} , respectively. This shows that if the Fe...Fe distance is kept fixed to 2.9 or 3.3 Å and the Fe–O_c–Fe angle is increased from 85° to 105° , J_{NN} decreases and becomes negative. On the other hand, if the Fe–O_c–Fe angle is fixed to 85° or 105° , and the Fe...Fe distance is increased from 2.9 Å to 3.3 Å, the J_{NN} value again decreases. Hence, changing either the Fe...Fe distance or the Fe–O_c–Fe angle has an effect on the magnetic coupling.

4. CONCLUSIONS

In contrast to $\text{Fe}_2(\text{dobdc})$, $\text{Fe}_2(\text{O})_2(\text{dobdc})$ and $\text{Fe}_2(\text{OH})_2(\text{dobdc})$ feature antiferromagnetic (AFM) coupling down each metal chain (Figure 10). Previous work by Bloch et

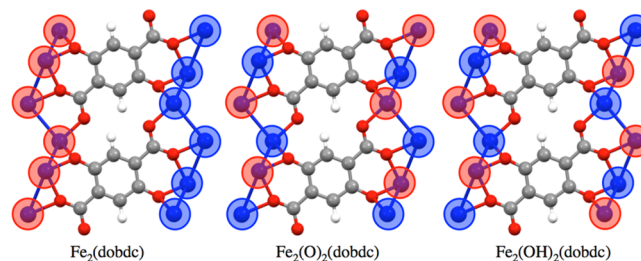


Figure 10. Representation of the spin configurations of the studied MOFs (atom legend: blue = Fe atoms, red = O atoms, gray = C atoms, and white = H atoms). Red circles indicate spin-up Fe spins and blue circles indicate spin-down Fe spins.

al.¹⁶ and calculations performed by Park et al.¹⁷ suggest that the shift from ferromagnetic (FM) to AFM coupling is the result of ligands changing the intrachain Fe...Fe distances and Fe–O–Fe angles. Here, we find that the effect can also be partially accounted for by the electronic effect of the ligands, the oxidation state of the metal centers, and/or the spin state of the metal centers, even in the absence of geometry changes. This indicates that structural and electronic changes upon framework oxidation likely act in concert to effect magnetic coupling.

The computationally efficient PBE+U and GAM+U approaches predict structural properties that agree quite well with the values obtained using more expensive hybrid functionals. Inclusion of damped dispersion effects by molecular mechanics does alter equilibrium volumes; however, the effect is minor when compared to the inclusion of Hartree–Fock exchange. Thus, rescaling PBE+U or GAM+U unit cells

and correcting for the electronic structure with single-point hybrid functional calculations appears to be an efficient approach to calculate magnetic properties of MOFs. Cluster models can be used to compute J_{NN} coupling values quite accurately, and can be used conveniently with a wider array of computational methods at a lower cost. However, capturing both the J_{NN} and J_{IC} magnetic coupling dependency on the MOF structure does require periodic calculations. Overall, theory can correctly describe the magnetic and electronic properties and their structural dependences for these materials, provided one is aware of the strengths and limitations of both periodic and cluster-based modeling. Ongoing research is directed toward predicting these properties for as-yet-unsynthesized materials.

■ ASSOCIATED CONTENT

■ Supporting Information

The Supporting Information is available free of charge on the ACS Publications website at DOI: 10.1021/acs.inorgchem.6b00467.

Equations that were used to extract the magnetic coupling parameters for the larger unit cell and the cluster model; the lattice parameters for all computed structures with all methods; the coordinates of the optimized structures using all methods; calculated bulk moduli for each MOF; computational and experimental infrared spectra; a k -points energy convergence test with $\text{Fe}_2(\text{dobdc})$; partial atomic charges; plots of the local density of states, including comparisons of all structures, computed with FM, AFM1, and AFM2 spin ordering (PDF)

■ AUTHOR INFORMATION

Corresponding Authors

*E-mail: joachim.paier@chemie.hu-berlin.de (J. Paier).

*E-mail: truhlar@umn.edu (D. G. Truhlar).

*E-mail: gagliardi@umn.edu (L. Gagliardi).

*E-mail: jrlong@berkeley.edu (J. R. Long).

Notes

The authors declare no competing financial interest.

■ ACKNOWLEDGMENTS

We thank Professor Joachim Sauer for insightful discussions and comments on the manuscript. This work was supported by the U.S. DOE, Office of Basic Energy Sciences, Division of Chemical Sciences, Geosciences and Biosciences (Award No. DE-FG02-12ER16362). This work has been carried out using the Minnesota Supercomputing Institute computational resources and National Energy Research Scientific Computing center resources and using computing time granted by the high-performance computer centers HLRN (North-German Supercomputing Alliance in Berlin and Hannover) and JUROPA (Forschungszentrum Jülich). J.P. acknowledges financial support by the Fonds der Chemischen Industrie (FCI). P.V. and J.B. acknowledge financial support by the Doctoral Dissertation Fellowship. L.E.D. and D.J.X. thank the National Science Foundation (NSF) for providing graduate fellowship support.

■ REFERENCES

(1) Dechambenoit, P.; Long, J. R. *Chem. Soc. Rev.* **2011**, *40*, 3249–3265.

(2) Kahn, O.; Larionova, J.; Yakhmi, J. V. *Chem.—Eur. J.* **1999**, *5*, 3443–3449.

(3) Shen, L.; Yang, S.-W.; Xiang, S.; Liu, T.; Zhao, B.; Ng, M.-F.; Goettlicher, J.; Yi, J.; Li, S.; Wang, L.; Ding, J.; Chen, B.; Wei, S.-H.; Feng, Y. P. *J. Am. Chem. Soc.* **2012**, *134*, 17286–17290.

(4) Mohapatra, S.; Rajeswaran, B.; Chakraborty, A.; Sundaresan, A.; Maji, T. K. *Chem. Mater.* **2013**, *25*, 1673–1679.

(5) Dzyaloshinsky, I. *J. Phys. Chem. Solids* **1958**, *4*, 241–255.

(6) Guha, B. C. *Nature* **1945**, *155*, 364–364.

(7) Goodenough, J. B. *Phys. Rev.* **1960**, *117*, 1442–1451.

(8) Odbadrakh, K.; Lewis, J. P.; Nicholson, D. M.; Petrova, T.; Michalkova, A.; Leszczynski, J. *J. Phys. Chem. C* **2010**, *114*, 3732–3736.

(9) Canepa, P.; Chabal, Y. J.; Thonhauser, T. *Phys. Rev. B: Condens. Matter Mater. Phys.* **2013**, *87*, 094407.

(10) Coudert, F.-X.; Ortiz, A. U.; Haigis, V.; Bousquet, D.; Fuchs, A. H.; Ballandras, A.; Weber, G.; Bezverkhy, I.; Geoffroy, N.; Bellat, J.-P.; Ortiz, G.; Chaplais, G.; Patarin, J.; Boutin, A. *J. Phys. Chem. C* **2014**, *118*, 5397–5405.

(11) Deria, P.; Mondloch, J. E.; Tylianakis, E.; Ghosh, P.; Bury, W.; Snurr, R. Q.; Hupp, J. T.; Farha, O. K. *J. Am. Chem. Soc.* **2013**, *135*, 16801–16804.

(12) Yu, D.; Yazaydin, A. O.; Lane, J. R.; Dietzel, P. D. C.; Snurr, R. Q. *Chem. Sci.* **2013**, *4*, 3544–3556.

(13) Haldoupis, E.; Borycz, J.; Shi, H. L.; Vogiatzis, K. D.; Bai, P.; Queen, W. L.; Gagliardi, L.; Siepmann, J. I. *J. Phys. Chem. C* **2015**, *119*, 16058–16071.

(14) Zhang, Q.; Li, B.; Chen, L. *Inorg. Chem.* **2013**, *52*, 9356–9362.

(15) Verma, P.; Xu, X.; Truhlar, D. G. *J. Phys. Chem. C* **2013**, *117*, 12648–12660.

(16) Bloch, E. D.; Queen, W. L.; Krishna, R.; Zadrozny, J. M.; Brown, C. M.; Long, J. R. *Science* **2012**, *335*, 1606–1610.

(17) Park, J.; Kim, H.; Jung, Y. *J. Phys. Chem. Lett.* **2013**, *4*, 2530–2534.

(18) Maurice, R.; Verma, P.; Zadrozny, J. M.; Luo, S.; Borycz, J.; Long, J. R.; Truhlar, D. G.; Gagliardi, L. *Inorg. Chem.* **2013**, *52*, 9379–9389.

(19) Xiao, D. J.; Bloch, E. D.; Mason, J. A.; Queen, W. L.; Hudson, M. R.; Planas, N.; Borycz, J.; Dzubak, A. L.; Verma, P.; Lee, K.; Bonino, F.; Crocellà, V.; Yano, J.; Bordiga, S.; Truhlar, D. G.; Gagliardi, L.; Brown, C. M.; Long, J. R. *Nat. Chem.* **2014**, *6*, 590–595.

(20) Verma, P.; Vogiatzis, K. D.; Planas, N.; Borycz, J.; Xiao, D. J.; Long, J. R.; Gagliardi, L.; Truhlar, D. G. *J. Am. Chem. Soc.* **2015**, *137*, 5770–5781.

(21) Wriedt, M.; Yakovenko, A. A.; Halder, G. J.; Prosvirin, A. V.; Dunbar, K. R.; Zhou, H. C. *J. Am. Chem. Soc.* **2013**, *135*, 4040–4050.

(22) Liechtenstein, A. I.; Anisimov, V. I.; Zaanen, J. *Phys. Rev. B: Condens. Matter Mater. Phys.* **1995**, *52*, R5467–R5470.

(23) Iori, F.; Gatti, M.; Rubio, A. *Phys. Rev. B: Condens. Matter Mater. Phys.* **2012**, *85*, 115129.

(24) Grau-Crespo, R.; Wang, H.; Schwingenschloegl, U. *Phys. Rev. B: Condens. Matter Mater. Phys.* **2012**, *86*, 081101.

(25) Henderson, T. M.; Paier, J.; Scuseria, G. E. *Phys. Status Solidi B* **2011**, *248*, 767–774.

(26) Moreira, I. P. R.; Illas, F. *Phys. Chem. Chem. Phys.* **2006**, *8*, 1645–1659.

(27) Bain, G. A.; Berry, J. F. *J. Chem. Educ.* **2008**, *85*, 532–536.

(28) Kahn, O. *Molecular Magnetism*; Wiley-VCH: New York, 1993; pp 257–258.

(29) Georges, R.; Borrás-Almenar, J. J.; Coronado, E.; Curély, J.; Drillon, M. *Magnetism: Molecules to Materials: Models and Experiments*; Wiley-VCH: Weinheim, Germany, 2002; Chapter 1, pp 1–47.

(30) Perdew, J. P.; Burke, K.; Ernzerhof, M. *Phys. Rev. Lett.* **1996**, *77*, 3865–3868.

(31) Yu, H. S.; Zhang, W.; Verma, P.; He, X.; Truhlar, D. G. *Phys. Chem. Chem. Phys.* **2015**, *17*, 12146–12160.

(32) Duanmu, K.; Luo, S.; Truhlar, D. G. *Minnesota—VASP Functional Module (MN-VFM – version 3.0)*; available via the Internet at: <http://comp.chem.umn.edu/mn-vfm/>.

- (33) Zhao, Y.; Truhlar, D. G. *J. Chem. Phys.* **2006**, *125*, 194101.
- (34) Zhao, Y.; Truhlar, D. G. *J. Chem. Phys.* **2009**, *130*, 130.
- (35) Booth, G. H.; Grüneis, A.; Kresse, G.; Alavi, A. *Nature* **2012**, *493*, 365–370.
- (36) Paier, J.; Ren, X.; Rinke, P.; Scuseria, G. E.; Grüneis, A.; Kresse, G.; Scheffler, M. *New J. Phys.* **2012**, *14*, 043002.
- (37) Cramer, C. J.; Truhlar, D. G. *Phys. Chem. Chem. Phys.* **2009**, *11*, 10757–10816.
- (38) Asmis, K. R.; Santambrogio, G.; Brümmer, M.; Sauer, J. *Angew. Chem.* **2005**, *117*, 3182–3185.
- (39) Chevrier, V. L.; Ong, S. P.; Armiento, R.; Chan, M. K. Y.; Ceder, G. *Phys. Rev. B: Condens. Matter Mater. Phys.* **2010**, *82*, 075122.
- (40) Cohen, A. J.; Mori-Sanchez, P.; Yang, W. *J. Chem. Phys.* **2007**, *126*, 191109.
- (41) Mori-Sanchez, P.; Cohen, A. J.; Yang, W. *Phys. Rev. Lett.* **2008**, *100*, 146401.
- (42) Manz, T. A.; Sholl, D. S. *J. Chem. Theory Comput.* **2011**, *7*, 4146–4164.
- (43) Krukau, A. V.; Vydrov, O. A.; Izmaylov, A. F.; Scuseria, G. E. *J. Chem. Phys.* **2006**, *125*, 224106.
- (44) Becke, A. D. *J. Chem. Phys.* **1993**, *98*, 5648–5652.
- (45) Lee, C. T.; Yang, W. T.; Parr, R. G. *Phys. Rev. B: Condens. Matter Mater. Phys.* **1988**, *37*, 785–789.
- (46) Vosko, S. H.; Wilk, L.; Nusair, M. *Can. J. Phys.* **1980**, *58*, 1200–1211.
- (47) Stephens, P. J.; Devlin, F. J.; Chabalowski, C. F.; Frisch, M. J. *J. Phys. Chem.* **1994**, *98*, 11623–11627.
- (48) Ernzerhof, M.; Scuseria, G. E. *J. Chem. Phys.* **1999**, *110*, 5029–5036.
- (49) Adamo, C.; Barone, V. *J. Chem. Phys.* **1999**, *110*, 6158–6170.
- (50) Zhao, Y.; Truhlar, D. G. *Theor. Chem. Acc.* **2008**, *120*, 215–241.
- (51) Kresse, G.; Furthmüller, J. *Phys. Rev. B: Condens. Matter Mater. Phys.* **1996**, *54*, 11169–11186.
- (52) Kresse, G.; Furthmüller, J. *Comput. Mater. Sci.* **1996**, *6*, 15–50.
- (53) Heyd, J.; Scuseria, G. E.; Ernzerhof, M. *J. Chem. Phys.* **2003**, *118*, 8207–8215.
- (54) Paier, J.; Marsman, M.; Hummer, K.; Kresse, G.; Gerber, I. C.; Angyan, J. G. *J. Chem. Phys.* **2006**, *124*, 154709.
- (55) Gygi, F.; Baldereschi, A. *Phys. Rev. B: Condens. Matter Mater. Phys.* **1986**, *34*, 4405–4408.
- (56) Onida, G.; Reining, L.; Rubio, A. *Rev. Mod. Phys.* **2002**, *74*, 601–659.
- (57) Heyd, J.; Scuseria, G. E. *J. Chem. Phys.* **2004**, *121*, 1187–1192.
- (58) Heyd, J.; Scuseria, G. E.; Ernzerhof, M. *J. Chem. Phys.* **2006**, *124*, 219906.
- (59) Rivero, P.; Moreira, I. d. P. R.; Illas, F.; Scuseria, G. E. *J. Chem. Phys.* **2008**, *129*, 184110.
- (60) Zhou, J.; Sun, Q. *J. Am. Chem. Soc.* **2011**, *133*, 15113–15119.
- (61) Grimme, S. *J. Comput. Chem.* **2006**, *27*, 1787–1799.
- (62) Bucko, T.; Hafner, J.; Lebegue, S.; Angyan, J. G. *J. Phys. Chem. A* **2010**, *114*, 11814–11824.
- (63) Kerber, T.; Sierka, M.; Sauer, J. *J. Comput. Chem.* **2008**, *29*, 2088–2097.
- (64) Penschke, C.; Paier, J.; Sauer, J. *J. Phys. Chem. C* **2013**, *117*, 5274–5285.
- (65) Blöchl, P. E. *Phys. Rev. B: Condens. Matter Mater. Phys.* **1994**, *50*, 17953–17979.
- (66) Kresse, G.; Joubert, D. *Phys. Rev. B: Condens. Matter Mater. Phys.* **1999**, *59*, 1758–1775.
- (67) Krivy, I.; Gruber, B. *Acta Crystallogr., Sect. A: Cryst. Phys., Diffr., Theor. Gen. Crystallogr.* **1976**, *32*, 297–298.
- (68) Grosse-Kunstleve, R. W.; Sauter, N. K.; Adams, P. D. *Acta Crystallogr., Sect. A: Found. Crystallogr.* **2004**, *60*, 1–6.
- (69) Gajdos, M.; Hummer, K.; Kresse, G.; Furthmüller, J.; Bechstedt, F. *Phys. Rev. B: Condens. Matter Mater. Phys.* **2006**, *73*, 045112.
- (70) Baroni, S.; de Gironcoli, S.; Dal Corso, A.; Giannozzi, P. *Rev. Mod. Phys.* **2001**, *73*, 515–562.
- (71) Born, M.; Huang, K. *Dynamical Theory of Crystal Lattices*; Oxford University Press: Oxford, U.K., 1954.
- (72) Pick, R. M.; Cohen, M. H.; Martin, R. M. *Phys. Rev. B* **1970**, *1*, 910.
- (73) Frisch, M. J.; Trucks, G. W.; Schlegel, H. B.; Scuseria, G. E.; Robb, M. A.; Cheeseman, J. R.; Scalmani, G.; Barone, V.; Mennucci, B.; Petersson, G. A.; Nakatsuji, H.; Caricato, M.; Li, X.; Hratchian, H. P.; Izmaylov, A. F.; Bloino, J.; Zheng, G.; Sonnenberg, J. L.; Hada, M.; Ehara, M.; Toyota, K.; Fukuda, R.; Hasegawa, J.; Ishida, M.; Nakajima, T.; Honda, Y.; Kitao, O.; Nakai, H.; Vreven, T.; Montgomery, J. A., Jr.; Peralta, J. E.; Ogliaro, F.; Bearpark, M. J.; Heyd, J.; Brothers, E. N.; Kudin, K. N.; Staroverov, V. N.; Kobayashi, R.; Normand, J.; Raghavachari, K.; Rendell, A. P.; Burant, J. C.; Iyengar, S. S.; Tomasi, J.; Cossi, M.; Rega, N.; Millam, N. J.; Klene, M.; Knox, J. E.; Cross, J. B.; Bakken, V.; Adamo, C.; Jaramillo, J.; Gomperts, R.; Stratmann, R. E.; Yazyev, O.; Austin, A. J.; Cammi, R.; Pomelli, C.; Ochterski, J. W.; Martin, R. L.; Morokuma, K.; Zakrzewski, V. G.; Voth, G. A.; Salvador, P.; Dannenberg, J. J.; Dapprich, S.; Daniels, A. D.; Farkas, Ö.; Foresman, J. B.; Ortiz, J. V.; Cioslowski, J.; Fox, D. J. *Gaussian 09; Revision D.01*; Gaussian, Inc.: Wallingford, CT, USA, 2013.
- (74) Weigend, F.; Ahlrichs, R. *Phys. Chem. Chem. Phys.* **2005**, *7*, 3297–3305.
- (75) Heisenberg, W. *Eur. Phys. J. A* **1928**, *49*, 619–636.
- (76) Dirac, P. A. M. *Proc. R. Soc. London, Ser. A* **1929**, *123*, 714–733.
- (77) Van Vleck, J. H. *Rev. Mod. Phys.* **1945**, *17*, 27–47.
- (78) Hamill, M. B.; Danilovic, D.; Yuen, T.; Li, K. H.; Li, J. *J. Appl. Phys.* **2012**, *111*, 07B332.
- (79) Borycz, J.; Lin, L.-C.; Bloch, E. D.; Kim, J.; Dzuba, A. L.; Maurice, R.; Semrouni, D.; Lee, K.; Smit, B.; Gagliardi, L. *J. Phys. Chem. C* **2014**, *118*, 12230–12240.
- (80) Bloch, E. D.; Murray, L. J.; Queen, W. L.; Chavan, S.; Maximoff, S. N.; Bigi, J. P.; Krishna, R.; Peterson, V. K.; Grandjean, F.; Long, G. J.; Smit, B.; Bordiga, S.; Brown, C. M.; Long, J. R. *J. Am. Chem. Soc.* **2011**, *133*, 14814–14822.
- (81) Hohenberger, J.; Ray, K.; Meyer, K. *Nat. Commun.* **2012**, *3*, 720.
- (82) Alecu, I. M.; Zheng, J.; Zhao, Y.; Truhlar, D. G. *J. Chem. Theory Comput.* **2010**, *6*, 2872–2887.
- (83) Huang, S.; Wilson, B. E.; Wang, B.; Fang, Y.; Buffington, K.; Stein, A.; Truhlar, D. G. *J. Am. Chem. Soc.* **2015**, *137*, 10992–11003.
- (84) Verdager, M.; Bleuzen, A.; Marvaud, V.; Vaissermann, J.; Seuleiman, M.; Desplanches, C.; Sculler, A.; Train, C.; Garde, R.; Gelly, G.; Lomenech, C.; Rosenman, I.; Veillet, P.; Cartier, C.; Villain, F. *Coord. Chem. Rev.* **1999**, *190–192*, 1023–1047.
- (85) Martin, R. L.; Illas, F. *Phys. Rev. Lett.* **1997**, *79*, 1539–1542.